Slave–Boson Approach to Strongly Correlated Electron Systems

H. Fehske, M. Deeg and H. Büttner

January 31, 1996

1 Slave–Boson Approach to Strongly Correlated Electron Systems

1.1 Introduction

The problem of understanding high–temperature superconductivity has been a challenge to theoreticans from a wide variety of fields. Many theoretical investigations have been carried out in order to identify the mechanism of this fascinating phenomenon as well as to establish the canonical model itself [1]. Although excellent progress is being made in deducing a consistent description of the high–T_c systems from a first–principles theory, at present no microscopic theory can account for their 'unconventional' normal–phase data as a whole. The interplay of charge and spin dynamics in the *normal state* seems to hold the key to the understanding of the physical mechanism behind high–T_c superconductivity in the cuprates. Both macroscopic measurements of transport and magnetic properties as well as microscopic measurements probing the charge and spin excitation spectra were fundamental in establishing the anomalous normal state properties of these materials [1].

The nature of spin excitations of the high–T_c cuprates has been experimentally studied by means of nuclear magnetic/quadrupole resonance (NMR/NQR) and inelastic neutron scattering (INS) techniques clarifying the persistence of strong antiferromagnetic (AFM) correlations in the normal and superconducting states [2]. Detailed investigations of the wave–vector dependence of the low–frequency spin fluctuation spectrum have revealed remarkable differences between the $\mathrm{YBa_2Cu_3O_{6+x}}$ and $\mathrm{La_{2-x}Sr_xCuO_4}$

families at low doping level x; the dynamic structure factor $S(\vec{q},\omega)$ keeps its maximum at (π,π) in the YBCO system, while in LSCO, the peaks are displaced from the commensurate position to the four incommensurate wave–vectors $\pi(1\pm q_o,1)$, $\pi(1,1\pm q_o)$, where $q_o\sim 2x$. On the other hand, the analysis of the NMR data shows that the relaxation rates on the planar Cu sites are similar in all materials. Two striking features are associated with ${}^{63}T_1^{-1}$: (i) as a result of strong local spin fluctuations on ^{63}Cu sites it is enhanced by an order of magnitude over the oxygen rate ${}^{17}T_1^{-1}$; and (ii) in sharp contrast to the Korringa–like behaviour at the planar ^{17}O sites, its temperature dependence does not follow the Korringa law [2].

The physical origin of the contrasting $\vec{q}$–dependence of the spin fluctuation spectrum is still under discussion. Millis and Monien [3] have argued that the spin dynamics and, in particular, the temperature dependence of the spin susceptibility $\chi_s(T)$ in LSCO are caused by a spin–density–wave instability, whereas in the YBCO family they are due to in–plane AFM fluctuations and a novel non–Fermi–liquid spin singlet pairing of electrons in adjacent planes. On the other hand, the magnetic properties are intimately related to the energy band dispersion of the noninteracting system within a Fermi liquid based framework, i.e., in this way the observed spin dynamics can be attributed to different Fermi–surface (FS) geometry of LSCO-type and YBCO–type, respectively. Along this line, details of the spin fluctuation spectrum are studied using a nearly antiferromagnetic Fermi–liquid approach by Monthoux and Pines [4]. From a more microscopic point of view, the important effects of FS shape on the magnetic properties were confirmed by Si *et al* [5] within a large Coulomb–U auxiliary and by Fukuyama and co–workers [6] on the basis of a resonating–valence–bond (RVB) slave–boson mean–field approach to the extended t–J model. Furthermore Ito *et al.* [7] have recently reported that the charge transport in the CuO_2 plane is determined by dominant spin scattering, i.e. the spin dynamics are manifest in the extraordinary transport properties of the high-T_c cuprates as well.

Encouraged by these findings it is the aim of this report to study magnetic and transport phenomena of high–T_c's in terms of the probably most simple effective one–band model describing both correlation and band structure effects, the so–called t–t'–J model:

$$\mathcal{H}_{t-t'-J} = -t\sum_{\langle i,j\rangle,\sigma}\tilde{c}^\dagger_{i\sigma}\tilde{c}_{j\sigma} - t'\sum_{\langle\langle i,j\rangle\rangle,\sigma}\tilde{c}^\dagger_{i\sigma}\tilde{c}_{j\sigma} + J\sum_{\langle ij\rangle}\left(\vec{S}_i\vec{S}_j-\frac{\tilde{n}_i\tilde{n}_j}{4}\right). \tag{1.1.1}$$

$\mathcal{H}_{t-t'-J}$ acts in a projected Hilbert space without double occupancy, where $\tilde{c}^{(\dagger)}_{i\sigma} = c^{(\dagger)}_{i\sigma}(1-\tilde{n}_{i-\sigma})$ is the electron annihilation (creation) operator, $\vec{S}_i =$

$\frac{1}{2}\sum_{\sigma\sigma'}\tilde{c}^{\dagger}_{i\sigma}\vec{\tau}_{\sigma\sigma'}\tilde{c}_{i\sigma'}$, and $\tilde{n}_i = \sum_{\sigma}\tilde{c}^{\dagger}_{i\sigma}\tilde{c}_{i\sigma}$. J measures the AFM exchange interaction, t and t' denotes hopping processes between nearest–neighbour (NN; $\langle i,j\rangle$) and next nearest–neighbour (NNN; $\langle\langle i,j\rangle\rangle$) sites on a square lattice. Compared to the original t–J model the t'–term incorporates several important effects near half–filling. Starting from a rather complex three–band Hubbard or Emery model model [8] for the CuO_2 planes, quantum cluster calculations [9] have revealed that the relative large direct transfer between NN oxygen sites ($t_{pp} \gtrsim t_{pd}/2$) leads to a sizeable NNN hopping t' in the context of an effective one–band description. More recently the t'–term has been introduced to reproduce the FS geometry observed in ARPES experiments [6, 10, 11, 12]. Fitting the quasiparticle dispersion relation

$$\varepsilon_{\vec{k}} = -2t(\cos k_x + \cos k_y) - 4t' \cos k_x \cos k_y \,, \tag{1.1.2}$$

involved in (1.1.1), to experimental and band theory results yields t in the order of 0.3 eV and, e.g., for the case of YBCO, $t' \simeq -0.4t$ [4, 5, 13]. Moreover, Tohyama and Maekawa [12] have emphasized that a t–t'–J model with $t' > 0$ can be used to describe the electron–doped systems, e.g. $Nd_{2-x}Ce_xCuO_4$ (NCCO). In this case one has to shift the momentum $\vec{k} \to \vec{k} + (\pi,\pi)$ [12], i.e., within a band–filling scenario one obtains a hole–pocket like FS centered at (π,π)–point which *shrinks* with increasing doping [14]. Finally, as pointed out by Lee [15], in a locally AFM environment doped holes can propagate coherently only on the same sublattice without disturbing spins. Therefore the t'– term coupling the same sublattice becomes crucial for the low–lying magnetic excitations. This clearly is a correlation effect related to the NNN hopping processes.

1.2 Slave–boson theory for the t–t'–J model

Apart from numerical techniques, the slave–particle methods have been employed extensively in studying the effects of electron–electron correlation in the (extended) t–J model [6, 16, 17, 18, 19, 20, 21]. The two commonly used approaches, the NZA slave–boson [16, 17] and slave–fermion [18] schemes, however, yield quite different results concerning the (mean–field) ground–state phase diagram and spin/charge excitations for this model [22]. As yet, the relationship between both types of slave–field theories is not well understood. Within the NZA formulation, for example, the Hamiltonian can be solved by a mean–field approximation with the (uniform) RVB order parameter. A serious difficulty of this approach is the absence of AFM correlations [18, 22], e.g., in the half–filled case, the lowest energy state, the energy of which is considerable higher than numerical estimates indicate, does not satisfy the Marshall sign rule and fails to show the expected long–range Néel order [23]. On the other hand, the mean–field slave–fermion schemes [18] are known to give reasonable results for the spin susceptibility as well as for the spin correlation length [21, 22], but also suffer from neglecting important correlation effects, especially the fermion charge degrees of freedom are not described sufficiently well. In contrast, the four–field slave–boson (SB) technique, introduced by Kotliar and Ruckenstein (KR) [24] in the context of the Hubbard model, has the advantage of treating spin and charge degrees of freedom on an equal footing. Starting from the scalar KR SB representation of the Hubbard model, one may 'generate' an intersite exchange interaction via a loop expansion in the coherent state functional integral [19]. However, the effective t–J Lagrangian, derived in this way, contains only an Ising interaction term, i.e., important spin–flip exchange processes are neglected. As we shall see below, to bosonize the complete exchange interaction term one has to use the spin–rotation–invariant (SRI) extension of the KR SB theory from the beginning [25, 26].

1.2.1 SU(2)–invariant slave–particle representation

For the sake of definiteness, we return to the extended t–J Hamiltonian (1.1.1), that may be cast into the form

$$\mathcal{H}_{t-J} = \sum_{i,j} t_{ij}\, \tilde{\Psi}_i^\dagger \tilde{\Psi}_j - \frac{J}{4} \sum_{\langle ij \rangle} \left(\tilde{\Psi}_i^\dagger \underline{\tau}^\mu \tilde{\Psi}_i \right) \left(\tilde{\Psi}_j^\dagger \underline{\tau}_\mu \tilde{\Psi}_j \right) . \tag{1.2.1}$$

In order to bring out the $SU(2)$ symmetry of the system, we have used in (1.2.1) a spinor representation, where the one–row [one–column] matrices $\tilde{\Psi}_i^\dagger = (\tilde{\Psi}_{i\sigma}^\dagger, \tilde{\Psi}_{i-\sigma}^\dagger)$ $[\tilde{\Psi}_i]$ are built up by the projected fermion creation [annihilation] operators $\tilde{\Psi}_{i\sigma}^\dagger \equiv \tilde{c}_{i\sigma}^\dagger$ $[\tilde{\Psi}_{i\sigma} \equiv \tilde{c}_i]$. $\underline{\tau}^\mu$ $[\underline{\tau}_\mu]$ denotes the kontravariant [kovariant] four–component vector ($\mu = 0, x, y, z$) of Pauli matrices. To preserve SRI, we apply to $\mathcal{H}_{t-J}$ the manifest $[SU(2) \otimes U(1)]$ invariant SB scheme [26, 27] based on the SRI SB approach developed for the Hubbard model by Li *et al.* [28]. Accordingly, we define scalar boson fields $e_i^{(\dagger)}$ and bosonic matrix operators $\underline{p}_i^{(\dagger)}$ (representing empty and singly occupied sites, respectively) and pseudofermion spinor fields $\Psi_i^{(\dagger)}$ in the following way:

$$\begin{aligned} |\, 0_i \rangle &= e_i^\dagger \, |vac\rangle \,, \\ |\, \sigma_i \rangle &= \sum_\rho \Psi_{i\rho}^\dagger p_{i\rho\sigma}^\dagger \, |vac\rangle \,. \end{aligned} \tag{1.2.2}$$

The unphysical states in the extended Fock space of pseudofermionic and bosonic states are eliminated by imposing two sets of *local* constraints:

$$C_i^{(1)} = e_i^\dagger e_i \ + 2\,\mathrm{Tr}\,\underline{p}_i^\dagger \underline{p}_i \ - 1 \ = 0\,, \tag{1.2.3}$$

expressing the completeness of the bosonic projectors, and

$$\underline{C}_i^{(2)} = \Psi_i \otimes \Psi_i^\dagger + 2\,\underline{p}_i^\dagger \underline{p}_i - \underline{\tau}_o = 0\,, \tag{1.2.4}$$

relating the pseudofermion number to the number of p–type slave bosons (hereafter underbars denote a 2×2 matrix in the spin variables). Obviously, double occupancy has been projected out. In the transformation of the fermionic spinor fields analogous to [28, 26],

$$\tilde{\Psi}_i \quad \longrightarrow \quad \underline{z}_i \Psi_i\,, \tag{1.2.5}$$

the nonlinear bosonic hopping operators

$$\underline{z}_i = [\underline{\tau}_o - 2\underline{p}_i^\dagger \underline{p}_i]^{-1/2}\, e_i^\dagger\, [1 + e_i^\dagger e_i + 2\,\mathrm{Tr}\,\underline{p}_i^\dagger \underline{p}_i]^{1/2}\, \underline{p}_i\, [(1 - e_i^\dagger e_i)\underline{\tau}_o - 2\underline{\tilde{p}}_i^\dagger \underline{\tilde{p}}_i]^{-1/2} \tag{1.2.6}$$

yield a correlation–induced band renormalization. Exploiting the $SU(2) \leftrightarrow O(3)$ homomorphism, the matrix operators $\underline{p}_i$ may be decomposed into scalar (singlet) $p_o^{(\dagger)}$ and vector (triplet) $\vec{p}_i = (p_{ix}, p_{iy}, p_{iz})$ components as

$$\underline{p}_i^{(\dagger)} = \frac{1}{2} \sum_\mu \underline{\tau}_\mu p_{i\mu}^{(\dagger)}\,, \tag{1.2.7}$$

where the $p_{i\mu}$ obey the usual Bose commutation rules $[p_{i\mu}, p_{j\mu'}^\dagger] = \delta_{ij}\delta_{\mu\mu'}$. Consequently, the pseudofermions $\Psi_i = (\Psi_{i\rho}, \Psi_{i-\rho})^T$ satisfy anticommutation relations of the form $\{\Psi_{i\rho}, \Psi_{j\rho'}^\dagger\} = \delta_{ij}\,\delta_{\rho\rho'}$.

This way the interaction term is converted due to

$$\tilde{\Psi}_i^\dagger \underline{\tau}_\mu \tilde{\Psi}_i \longrightarrow 2\,\mathrm{Tr}\,\underline{p}_i^\dagger \underline{\tau}_\mu \underline{p}_i\,, \tag{1.2.8}$$

where, more explicitly, the locally defined particle number and spin operators are just

$$\begin{aligned} \tilde{n}_i \quad &\longrightarrow \quad \tilde{n}_i(p_{i\mu}) = 2\,\mathrm{Tr}\,\underline{p}_i^\dagger \underline{p}_i = \sum_\mu p_{i\mu}^\dagger p_{i\mu}\,, \\ \vec{S}_i \quad &\longrightarrow \quad \vec{S}_i(p_{i\mu}) = \mathrm{Tr}\,\underline{p}_i^\dagger \vec{\underline{\tau}} \underline{p}_i = \frac{1}{2}\left(p_{io}^\dagger \vec{p}_i + \vec{p}_i^{\,\dagger} p_{io} - i\,\vec{p}_i^{\,\dagger} \times \vec{p}_i\right). \end{aligned} \tag{1.2.9}$$

Actually, the components of the bosonized SB spin operator act as generators of rotations in spin space, i.e., $\vec{S}_i(p_{i\mu})$ satisfies the spin algebra. Since

$C_i^{(1)}$ and $\underline{C}_i^{(2)}$ commute with the SB t–J Hamiltonian, the constraints (1.2.3) and (1.2.4) can be ensured by introducing the *time–independent* Lagrange multipliers $\lambda_i^{(1)}$ and $\underline{\lambda}_i^{(2)} = \sum_\mu \underline{\tau}_\mu \lambda_{i\mu}^{(2)}$.[1] As a consequence, the Hamiltonian of the t–J model (1.2.1) in terms of the slave–boson and pseudofermion operators has to be replaced by

$$\begin{aligned} \mathcal{H}_{t-J}^{SB} &= \sum_{i,j} t_{ij} \Psi_i^\dagger \underline{z}_i^\dagger \underline{z}_j \Psi_j - J \sum_{\langle ij \rangle} \left(\mathrm{Tr}\, \underline{p}_i^\dagger \underline{\tau}^\mu \underline{p}_i \right) \left(\mathrm{Tr}\, \underline{p}_j^\dagger \underline{\tau}_\mu \underline{p}_j \right) \\ &\quad + \sum_i \left(\lambda_i^{(1)} C_i^{(1)} + \mathrm{Tr}\, \underline{\lambda}_i^{(2)} \underline{C}_i^{(2)} \right) . \end{aligned} \tag{1.2.10}$$

In the physical subspace, $\mathcal{H}_{t-J}^{SB}$ posses the same matrix elements for the basis states (1.2.2) as the original t–J Hamiltonian (1.2.1) for the purely fermionic states. To verify this directly, special attention has to be paid to the bosonization of AFM exchange interaction term

$$\left(\tilde{\Psi}_i^\dagger \underline{\tau}^\mu \tilde{\Psi}_i \right) \left(\tilde{\Psi}_j^\dagger \underline{\tau}_\mu \tilde{\Psi}_j \right) = 2 \sum_\sigma \left(\tilde{c}_{i\sigma}^\dagger \tilde{c}_{j-\sigma}^\dagger \tilde{c}_{j\sigma} \tilde{c}_{i-\sigma} - \tilde{c}_{i\sigma}^\dagger \tilde{c}_{j-\sigma}^\dagger \tilde{c}_{j-\sigma} \tilde{c}_{i\sigma} \right), \tag{1.2.11}$$

which includes besides the Ising exchange contributions ($|\downarrow_i \uparrow_j\rangle \leftrightarrow |\downarrow_i \uparrow_j\rangle$) the spin–flip processes ($|\downarrow_i \uparrow_j\rangle \leftrightarrow |\uparrow_i \downarrow_j\rangle$). Let us emphasize that the matrix elements of the spin–flip terms are *not* reproduced in the scalar KR SB approach [19]. By contrast, within the SRI SB approach it is a straightforward exercise to show that these contributions can be expressed in terms of the $p_{i\rho\rho'}^{(\dagger)}$:

$$\sum_{\rho\rho'} p_{i\rho\sigma}^\dagger \, p_{j\rho'-\sigma}^\dagger \, p_{j\sigma\rho'} \, p_{i-\sigma\rho} \, |-\sigma_i \; \sigma_j\rangle = \frac{1}{4} \, |\sigma_i \; -\sigma_j\rangle \, . \tag{1.2.12}$$

Thus our SRI SB scheme (1.2.2)–(1.2.10) provides a consistent bosonization of the extended t–J model.

1.2.2 Functional integral formulation

To proceed further, it is convenient to represent the grand canonical partition function for the redefined SB Hamiltonian (1.2.10) in terms of a coherent–state functional integral [29] over Grassmann fermionic and complex bosonic fields as

$$\mathcal{Z} = \int \mathcal{D}[\bar{\Psi}_\rho, \Psi_\rho] \, \mathcal{D}[e^*, e] \, \mathcal{D}[p_\mu^*, p_\mu] \, d[\lambda^{(1)}] \, d[\lambda_\mu^{(2)}] \, e^{-\int_0^\beta d\tau \mathcal{L}(\tau)} , \tag{1.2.13}$$

[1] Note that additional constraints do not exist. Especially, if the constraint $\vec{p}_i \times \vec{p}_i = 0$ is added [25], the spin algebra is not satisfied.

$$\begin{aligned}
\mathcal{L}(\tau) &= \sum_i \Big(e_i^*(\partial_\tau + \lambda_i^{(1)})e_i + 2\,\mathrm{Tr}\,\underline{p}_i^{*T}[(\partial_\tau + \lambda_i^{(1)})\underline{\tau}_o - \underline{\lambda}_i^{(2)^T}]\underline{p}_i{}^T - \lambda_i^{(1)} \Big) \\
&\quad + J\sum_{\langle ij\rangle} \Big(\mathrm{Tr}\,\underline{p}_i^*\vec{\underline{\tau}}\underline{p}_i \cdot \mathrm{Tr}\,\underline{p}_j^*\vec{\underline{\tau}}\underline{p}_j - \mathrm{Tr}\,\underline{p}_i^*\underline{p}_i\,\mathrm{Tr}\,\underline{p}_j^*\underline{p}_j \Big) \\
&\quad + \sum_i \bar{\Psi}_i \Big((\partial_\tau - \mu)\underline{\tau}_o + \underline{\lambda}_i^{(2)} \Big) \Psi_i + \sum_{i,j} t_{ij}\bar{\Psi}_i \underline{z}_i^* \underline{z}_j \Psi_j \,, \qquad (1.2.14)
\end{aligned}$$

Apart from the above symmetry considerations the SB functional–integral formalism reveals additional global and local gauge invariances [25, 30, 31, 32]. The action $\mathcal{S} = \int_0^\beta d\tau \mathcal{L}(\tau)$ is invariant under the following site– and time–dependent phase transformations ($\theta_i(\tau)$ $\underline{\chi}_i(\tau)$), i.e., under the local symmetry group $SU(2)\otimes U(1)$,

$$\begin{aligned}
\Psi_i &\rightarrow e^{-i\theta_i}\, e^{i\underline{\chi}_i}\, \Psi_i \,, \\
e_i &\rightarrow e_i\, e^{-i\theta_i} \,, \\
\underline{p}_i &\rightarrow \underline{p}_i\, e^{-i\underline{\chi}_i} \,, \qquad (1.2.15)
\end{aligned}$$

provided that the (five) Lagrange parameters act as *time–dependent* gauge fields, $\lambda_i^{(1)}(\tau)$ and $\underline{\lambda}_i^{(2)}(\tau)$, absorbing the time derivatives of the phase factors:

$$\begin{aligned}
\lambda_i^{(1)} &\rightarrow \lambda_i^{(1)} + i\dot{\theta}_i \,, \\
\underline{\lambda}_i^{(2)} &\rightarrow e^{i\underline{\chi}_i}\, \underline{\lambda}_i^{(2)}\, e^{-i\underline{\chi}_i} - i\dot{\underline{\chi}}_i + i\dot{\theta}_i \underline{\tau}_o \,. \qquad (1.2.16)
\end{aligned}$$

Next, in the continuum limit, the radial gauge is introduced by representing the Bose fields by modulus and phase,

$$\begin{aligned}
e_i &= |e_i| e^{i\varphi(e_i)} \,, \\
\underline{p}_i &= \frac{1}{2}\sum_\mu \underline{\tau}_\mu |p_{i\mu}| e^{i\underline{\phi}(\underline{p}_i)} \,, \qquad (1.2.17)
\end{aligned}$$

(for a time discretized version of this gauge fixing, see [31]). Exploiting the gauge freedom of the action, we can now fix the five real–valued coefficients $\theta_i(\tau)$ $\chi_{i\mu}(\tau)$ to remove five phases ($\varphi_i(\tau)$, $\phi_{i\mu}(\tau)$) of the Bose fields e_i, $p_{i\mu}$ in the radial gauge. As a consequence *all* the Bose fields $\{e_i,\, p_{i\mu}\}$ become *real*, in contrast to the Hubbard model, where one SB field remains complex [25, 32]. At this point one should notice that the particle number and spin operators are changed into $\tilde{n}_i(p_{i\mu}) = \sum_\mu p_{i\mu}^2$, $\vec{S}_i(p_{i\mu}) = p_{io}\vec{p}_i$ (the previous notations e_i, p_{io} and $\vec{p}_i$ now denote the radial parts of the corresponding Bose fields). Then, using the familiar identity for Gaussian integrals over Grassmann fields [29],

$$\int \mathcal{D}[\bar{\Psi}_\rho, \Psi_\rho]\, e^{-\sum \bar{\Psi}_\rho [-G^{-1}]_{\rho\rho'} \Psi_\rho} = e^{\,\mathrm{Tr}\ln[-\underline{G}^{-1}]}\,, \tag{1.2.18}$$

the fermionic degrees of freedom can be integrated out, and we obtain the following exact representation of the grand canonical partition function

$$\mathcal{Z} = \int \mathcal{D}[\Phi]\, e^{-\mathcal{S}_{eff}} \tag{1.2.19}$$

in terms of the real–valued bosonic fields $\phi_{i\alpha}$,

$$\Phi_i(\tau) = (\phi_{i\alpha}(\tau)) = (e_i, p_{io}, \lambda_{io}^{(2)}, \lambda_i^{(1)}; p_{ix}, \lambda_{ix}^{(2)}; p_{iy}, \lambda_{iy}^{(2)}; p_{iz}, \lambda_{iz}^{(2)}). \tag{1.2.20}$$

In (1.2.19) the effective bosonic action $\mathcal{S}_{eff}$ takes the form

$$\begin{aligned}
\mathcal{S}_{eff} \;=\; & \int_0^\beta d\tau \Bigg\{ \sum_i \left[\lambda_i^{(1)} e_i^2 + \sum_\mu \left(\lambda_i^{(1)} - \lambda_{io}^{(2)} \right) p_{i\mu}^2 - 2 p_{io} \vec{p}_i \cdot \vec{\lambda}_i^{(2)} - \lambda_i^{(1)} \right] \\
& + J \sum_{\langle ij \rangle} \left[p_{io} \vec{p}_i \cdot \vec{p}_j p_{jo} - \frac{1}{4} \left(p_{io}^2 + \vec{p}_i^{\,2} \right) \left(p_{jo}^2 + \vec{p}_j^{\,2} \right) \right] \Bigg\} \\
& - \mathrm{Tr}_{ij,\rho\rho',\tau\tau'} \ln \left[- G^{-1}_{ij,\rho\rho'}(\tau,\tau') \right] ,
\end{aligned} \tag{1.2.21}$$

where the (inverse) SB Green propagator is given by

$$\begin{aligned}
G^{-1}_{ij,\rho\rho'}(\tau,\tau') \;=\; & \left[\left(-\partial_\tau + \mu - \lambda_{io}^{(2)} \right) \delta_{\rho\rho'} - \vec{\lambda}_i^{(2)} \cdot \vec{\tau}_{\rho\rho'} \right] \delta_{ij}\, \delta(\tau - \tau') \\
& - t_{ij} \, (\underline{z}_i^\dagger \underline{z}_j)_{\rho\rho',\tau\tau'} (1 - \delta_{ij}) \,.
\end{aligned} \tag{1.2.22}$$

It may be remarked that since the bosons $e_i(\tau)$ and $p_{i\mu}(\tau)$ are taken to be real, their kinetic terms, being proportional to the time derivatives in Eq. (1.2.14), drop out due to the periodic boundary conditions imposed on Bose fields ($\phi_{i\alpha}(\beta) = \phi_{i\alpha}(0)$). Strictly speaking it follows from this property that *all* the Bose fields do no longer have dynamics of their own [25].

1.2.3 Saddle–point approximation

The evaluation of (1.2.21) proceeds via the saddle–point expansion[2], where at the first level of approximation we look for an extremum $\overline{\mathcal{S}}(\overline{\Phi}_i)$ of the

[2] Mean–field approximations to the functional integral are achieved by replacing the bosonic fields by their time averaged values. For the Hubbard model, a comparison of the paramagnetic and antiferromagnetic SB solutions with quantum Monte Carlo results shows that such a mean–field like approach yields an excellent quantitative agreement for local observables [33] and therefore can give a qualitative correct picture with relatively little effort.

bosonized action $\mathcal{S}_{eff}$ with respect to the Bose and Lagrange multiplier fields $\phi_{i\alpha}$:

$$\frac{\partial \mathcal{S}_{eff}}{\partial \phi_{i\alpha}} \stackrel{!}{=} 0 \quad \Longrightarrow \quad \overline{\mathcal{S}} = \mathcal{S}_{eff}\Big|_{\Phi_i = \overline{\Phi}_i} . \tag{1.2.23}$$

The physically relevant saddle–point $\overline{\Phi}_i$ is determined to give the lowest *free energy* (per site)

$$\overline{f}_{t-J} = \overline{\Omega}/N + \mu n \, , \tag{1.2.24}$$

where at given mean electron density $n = 1 - \delta$, the chemical potential μ is fixed by the requirement

$$n = -\frac{1}{N}\frac{\partial \overline{\Omega}}{\partial \mu} \tag{1.2.25}$$

($\overline{\Omega} = \overline{\mathcal{S}}/\beta$ denotes the grand canonical potential). Obviously, an unrestricted minimization of the free energy functional is impossible for an infinite system. To keep the problem tractable, we use the ansatz

$$\vec{m}_i = m\vec{u}_i \, , \qquad \vec{u}_i = (\cos\vec{Q}\vec{R}_i, \sin\vec{Q}\vec{R}_i, 0) \tag{1.2.26}$$

for the local magnetization $\vec{m}_i = -2\vec{S}_i = -2p_{io}\vec{p}_i$. Following earlier analyses of spiral states for the Hubbard model [34] the unit vector $\vec{u}_i$ is chosen as a local spin quantization axis pointing in opposite directions on different sublattices. Thereby, the 'order parameter' wave–vector $\vec{Q}$ is introduced as a new 'variational' parameter to describe several magnetic ordered states: PM, FM ($\vec{Q} = 0$), AFM ($\vec{Q} = (\pi,\pi)$), and incommensurate (1,1)–spiral ($\vec{Q} = (Q,Q)$), $(1,\pi)$–spiral ($\vec{Q} = (Q,\pi)$) and (0,1)–spiral ($\vec{Q} = (0,Q)$) states. Note that since fluctuations of the charge density are not incorporated, the scalar Bose fields are homogeneous: $e_i = e$, $p_{io} = p_o$, $\lambda_i^{(1)} = \lambda^{(1)}$, and $\lambda_{io}^{(2)} = \lambda_o^{(2)}$. The vector fields exhibit the same spatial variation as the magnetization: $\vec{p}_i = p\vec{u}_i$ and $\vec{\lambda}_i^{(2)} = \lambda^{(2)}\vec{u}_i$. Then, transforming (1.2.21) in the $(\vec{k},\omega)$–representation, the trace in $\mathcal{S}_{eff}$ can be easily performed to give the free energy functional

$$\begin{aligned} f_{t-J} \quad = \quad & \lambda^{(1)}\left(e^2 + p_o^2 + p^2 - 1\right) - \lambda_o^{(2)}\left(p_o^2 + p^2\right) - 2\lambda^{(2)}p_o p + \mu n \\ & + J\left[p_o^2 p^2\left(\cos Q_x + \cos Q_y\right) - \frac{1}{2}\left(p_o^2 + p^2\right)^2\right] \\ & + \frac{1}{\beta N}\sum_{\vec{k}\nu}\ln\left[1 - n_{\vec{k}\nu}\right] , \end{aligned} \tag{1.2.27}$$

where

$$n_{\vec{k}\nu} = [\exp\{\beta(E_{\vec{k}\nu} - \mu)\} + 1]^{-1} \tag{1.2.28}$$

holds. The renormalized single–particle energies $E_{\vec{k}\nu}$ ($\nu = \pm$) obtained by diagonalizing the kinetic part of (1.2.21) [26]. Requiring that f_{t-J} be stationary with respect to the variation of the magnetic order vector, the wave–vector $\vec{Q}$ can be obtained from the 'extremal' condition

$$\sin Q_{x,y} = \frac{1}{J\, p_o^2 p^2}\, \frac{1}{N} \sum_{\vec{k}\nu} n_{\vec{k}\nu}\, \frac{\partial E_{\vec{k}\nu}}{\partial Q_{x,y}}\ . \tag{1.2.29}$$

If one substitutes (1.2.29) together with $\overline{\phi}_\alpha$ (obtained from the solution of the coupled self–consistency equations (1.2.23)) and (1.1.2) into (1.2.27), the free energy of the t–t'–J model is obtained as

$$\begin{aligned} \overline{f}_{t-t'-J} &= \frac{J}{4}\left[m^2\left(\cos Q_x + \cos Q_y\right) - 2n^2\right] + \lambda^{(2)} m + (\mu - \lambda_o^{(2)}) n \\ &\quad - \frac{1}{\beta N} \sum_{\vec{k}\nu} \ln\left[1 + e^{-\beta(E_{\vec{k}\nu} - \mu)}\right]\ , \end{aligned} \tag{1.2.30}$$

where the quasiparticle energy $E_{\vec{k}\nu}$ takes on the form

$$\begin{aligned} E_{\vec{k}\pm} &= \delta(1+\delta)(\varepsilon_{\vec{k}} + \varepsilon_{\vec{k}-\vec{Q}})/y + \lambda_o^{(2)} \\ &\quad \pm \left[\delta^2(\varepsilon_{\vec{k}} - \varepsilon_{\vec{k}-\vec{Q}})^2/y + [m(\varepsilon_{\vec{k}} + \varepsilon_{\vec{k}-\vec{Q}})/y + \lambda^{(2)}]^2\right]^{1/2} \end{aligned} \tag{1.2.31}$$

with $m = 2p_o p$ and $y = (1+\delta)^2 - m^2$.

In particular, at the spatially uniform paramagnetic saddle–point, $\overline{\Phi}^{(PM)} = (e, p_o, \lambda_o^{(2)}, \lambda^{(1)}; 0, 0; 0, 0; 0, 0)$, the remaining bosonic fields

$$\begin{aligned} e^2 &= \delta\ , \\ p_o^2 &= 1 - \delta\ , \\ \lambda^{(1)} &= -\frac{2 + 3\delta - \delta^2}{1 - \delta^2}\, \tilde{\varepsilon}(0)\ , \\ \lambda_o^{(2)} &= -\frac{2}{(1+\delta)^2}\, \tilde{\varepsilon}(0) - (1-\delta) J\ , \end{aligned} \tag{1.2.32}$$

are explicitly given in terms of J, δ and a single energy parameter $\tilde{\varepsilon}(0)$ defined by

$$\tilde{\varepsilon}(\vec{q}) = \frac{2}{N} \sum_{\vec{k}} \varepsilon_{\vec{k}-\vec{q}}\, \theta(\mu - E_{\vec{k}}) \tag{1.2.33}$$

(at $T = 0$). Here, the quasiparticle energy $E_{\vec{k}}$ is

$$E_{\vec{k}} = 2\delta\varepsilon_{\vec{k}}/(1+\delta) + \lambda_o^{(2)}\,, \tag{1.2.34}$$

and μ can be determined from $\delta = 1 - \frac{2}{N}\sum_{\vec{k}}\theta(\mu - E_{\vec{k}})$. Finally, in this approximation, the free energy becomes simply

$$\overline{f}_{t-J}^{(PM)} = z^2\tilde{\varepsilon}(0) - \frac{1}{2}J(1-\delta)^2 + \mu(1-\delta)\,. \tag{1.2.35}$$

1.2.4 Magnetic phase diagram of the t–t'–J model

In the numerical evaluation of the self–consistency loop we proceed as follows: at given model parameters J and δ, we solve the remaining saddle–point equations for m, $\lambda^{(1)}$, $\lambda_o^{(2)}$ and $\lambda^{(2)}$ together with the integral equation for μ using an iteration technique. Then, in an outer loop, the order parameter wave–vector $\vec{Q}$ is obtained from the extremal equation (1.2.29) by means of a secant method. Convergence is achieved if all quantities are determined with relative error less than 10^{-6}. Note that our numerical procedure allows for the investigation of different *metastable* symmetry broken states corresponding to *local* minima of the variational free energy functional (1.2.30).

Let us first consider the case $t' = 0$, i.e., the pure t–J model. The resulting ground–state phase diagram in the J–δ plane is shown in Fig. 1.1. For the case $\delta = 0$ (Heisenberg model), we obtain an AFM ground state.

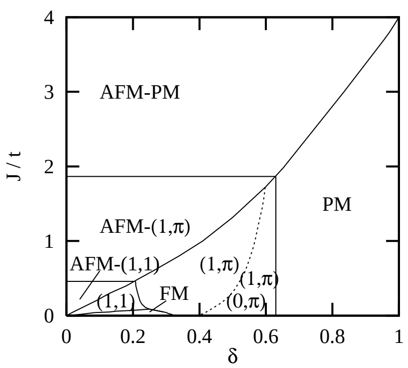

Abb. 1.1: SB ground–state phase diagram of the t–J model.

At $J = 0$, the FM is lowest in energy up to a hole concentration of 0.327, where a first order transition to the $(1,\pi)$–spiral takes place; above $\delta = 0.39$, we find a degenerate ground state with wave–vector $(0,\pi)$. At $\delta = 0.63$ the PM becomes the lowest in energy state (second order transition).

This coincides with the $U \to \infty$ SB results of the Hubbard model ($J = 4t^2/U$) [35]. The PM–FM instability occurs at $\delta_{PM-FM} = 0.33$ [32]. In contrast, the slave–fermion phase diagram [20] exhibits a much larger FM region. This can be taken as an indication that correlation effects are treated less accurate within the slave–fermion mean–field scheme [20, 36]. For finite exchange interaction J the (1,1)–spiral is the ground state at small doping. With increasing δ a transition to the FM takes place, which becomes unstable against the $(1, \pi)$–spiral at larger doping concentrations. For $J/t > 0.08$, we find a transition from (1,1)– to $(1, \pi)$–spirals at about $\delta \approx 0.2$. In Fig. 1.1, the dotted line separates the $(1, \pi)$–spiral state from the region, where the $(1, \pi)$ and $(0, \pi)$ states are degenerate. If we admit only homogeneous phases, the phase boundaries (1,1)–spiral$\rightleftharpoons$ $(1, \pi)$–spiral at $\delta \approx 0.2$ and $(1, \pi)/(0, \pi)$–phase$\rightleftharpoons$ PM at $\delta \approx 0.63$ remain nearly unchanged at larger values of J. However, analyzing the thermodynamic stability of the saddle–point solutions (i.e. the curvature of $\overline{f}_{t-J}(\delta)$), one observes a tendency towards phase separation into hole–rich and AFM regions above the 'diagonal' solid curve in the left upper part of the J–δ phase diagram (see below).

Figure 1.2.4 displays the variation of the 'extremal' spiral wave–vector $\vec{Q}$ as function of doping. At $\delta = 0$, $\vec{Q} = (\pi, \pi)$ indicates the AFM order. At low

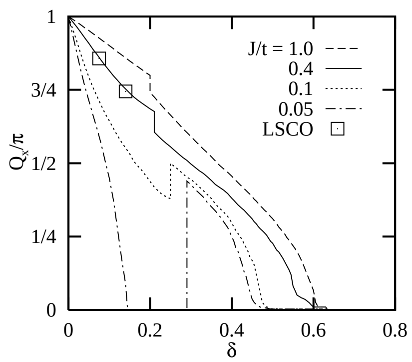

Abb. 1.2: The x–component of the spiral wave–vector $\vec{Q}$ as a function of doping δ (compared with experiments [□] on LSCO [37]).

doping the (1,1)–spiral order vector decreases approximately linear. With decreasing J the AFM exchange is weakened, consequently the deviation of the order vector from (π, π) increases. The discontinuities reflect the first order transition from (1,1)– to $(1, \pi)$–spirals. For $J/t = 0.05$ the transition to the FM state takes place, with Q_x jumping down to zero. The $(1, \pi)$–spiral wave–vector shows a monotonous decrease of Q_x until at $\delta = 0.63$ the transition to the PM ($Q_x = 0$) occurs. Comparing the magnitude of the theoretical order vector of the spiral solutions to results from inelastic neutron scattering experiments on $La_{2-x}Sr_xCuO_4$ [37], we find good agreement for an exchange interaction strength of $J/t = 0.4$ (which seems to be a reasonable value with respect to the strong electron correlations observed in the high–T_c's).

Next, we investigate the ground–state properties of the t–t'–J model, where we fix $J/t = 0.4$. Comparing the free energies of several (homoge-

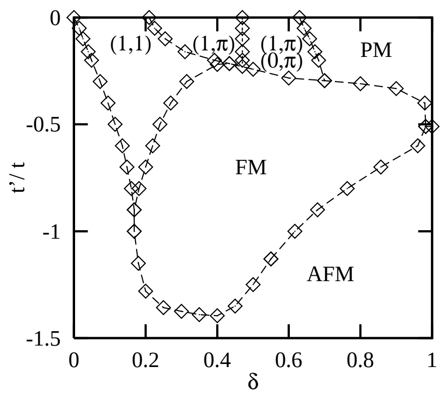

Abb. 1.3: Restricted SB ground–state phase diagram of the 2D t–t'–J model at $J/t = 0.4$.

neous) symmetry broken states, we obtain the SB phase diagram shown in the t'/t–δ plane in Fig. 1.3. Obviously, we can distinguish two regimes. In the parameter region $|t'/t| \lesssim 0.2$, Fig. 1.3 resembles the ground–state phase diagram of the pure t–J model (Fig. 1.1), i.e., we found large regions with incommensurate spiral order. However, compared to the pure t–J model, the t'–term stabilizes Néel order in a finite δ–region near half–filling. The increasing stability of AFM configurations can be intuitively understood because the t'–term moves electrons without disturbing the Néel–like background [12]. For larger ratios $|t'/t|$ we have a completely different situation. In this parameter regime only commensurate states (AFM, FM, PM) occur, where for $t' < t'_c = -1.4t$ we obtain the AFM state for all δ. Note the rather large differences to the value of t'_c obtained within a semiclassical $(1/N)$–expansion [38]. By varying the exchange coupling J the phase boundaries in the t'/t–δ plane are not much affected, e.g. for $J/t = 1$ and $t'/t = -0.4$, the transitions AFM$\rightleftharpoons$(1,1)–spiral and (1,1)–spiral$\rightleftharpoons$FM take place at $\delta = 0.17$ and $\delta = 0.6$, respectively. We would like to point out here that the main qualitative features of our SB phase diagram confirm recent studies of magnetic long–range order in the t–t'–J model [38, 39].

In Fig. 1.4 we plot the order parameter wave–vector as a function of doping at $t'/t = \pm 0.16$ and $t'/t = -0.4$. The behaviour of Q_x reflects a series of transitions AFM$\rightleftharpoons$(1,1)–spiral$\rightleftharpoons$ $(1,\pi)$–spiral$\rightleftharpoons$PM. The corresponding (sublattice–) magnetization abruptly changes at the (1,1)–spiral$\rightleftharpoons$ $(1,\pi)$–spiral first order transition. From Fig. 1.4 the asymmetry between hole

($t' < 0$) and electron doping ($t' > 0$) becomes evident. In contrast to recent Hartree–Fock results for the Hubbard model [40] we found the AFM phase near half–filling for both electron–doped and hole–doped cases (provided $t' \neq 0$). In the absence of t'–hopping, for arbitrarily small doping the AFM is found to be unstable against the (1,1)–spiral phase (cf. Fig. 1.3). Obviously, the AFM correlations are strongly enhanced by a positive t'–term, which is also in qualitative agreement with exact diagonalization studies of the t–t'–J model [12] and confirms the experimental findings for the electron–doped system NCCO [41, 42]. Note that the stability region of the

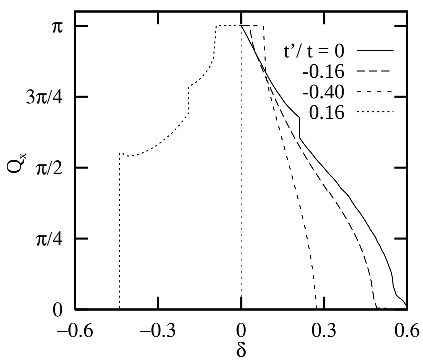

Abb. 1.4: The x–component of the SB spiral wave–vector $\vec{Q}$ away from half–filling for the negative values $t'/t = -0.16$ (solid) and $t'/t = -0.4$ (long–dashed), i.e., hole doping ($\delta > 0$), and for the positive one $t'/t = 0.16$ (dashed), i.e., electron doping.

AFM phase agrees surprisingly well with the combined phase diagram for $La_{2-x}Sr_xCuO_4$ and $Nd_{2-x}Sr_xCuO_4$ obtained from neutron scattering [43] and muon spin relaxation measurements [44], respectively. For the YBCO–parameter $t'/t = -0.4$, the AFM disappears around $\delta = 0.1$ whereas in the phase diagram of YBCO, determined by neutron diffraction [45], this transition takes place at about $x = 0.4$ *oxygen* content. However, there exits strong evidence that at least up to $x = 0.2$ *no holes* are transferred from CuO chains to CuO_2 –planes.

As we have already noted, the phase diagrams presented in Figs. 1.1 and 1.3 result from the relative stability of various *homogeneous* states. On the other hand, there are arguments for the existence of *inhomogeneous*, e.g., phase–separated states in the t–J and related models [46]. Using very different methods, it was realized by several groups [47, 48, 49, 50, 51], that at large J/t the ground state of the t–J model separates into hole–poor (AFM) and hole–rich regions. Unfortunately, in the physically interesting regime of small exchange coupling ($J/t \sim 0.2$–0.4) and low doping level this point is still controversial. To gain more insight into the phenomenon of phase separation in t–J–type models of strongly correlated electrons it seems to be important to investigate the effect of an additional NNN hopping term t' as well. Therefore we study the free energy as a function of hole density δ, where a (concave) convex curvature indicates local thermodynamic (in)stability implying a (negative) positive inverse isothermal compressibility $\kappa^{-1} = n^2 \frac{\partial^2 f}{\partial n^2}$. If $\kappa^{-1} < 0$, the domain of the two–phase regime is determined performing a Maxwell construction for the anomalous increase of the chemical potential μ by doping.

The results of our analysis of thermodynamic stability are depicted in Figs. 1.5 (a) and (b) for the t–J and t–t'–J model, respectively. The boundary of phase separation for the t–J model is given by the solid curve in the J–δ plane shown in Fig. 1.5 (a). As can be seen from Fig. 1.1, the different phase separated domains are built up by the (AFM) states at half–filling ($\delta = 0$) and the corresponding hole–rich state on the right boundary of the respective region. At $J = 0$, where we recover the $U \to \infty$ result of

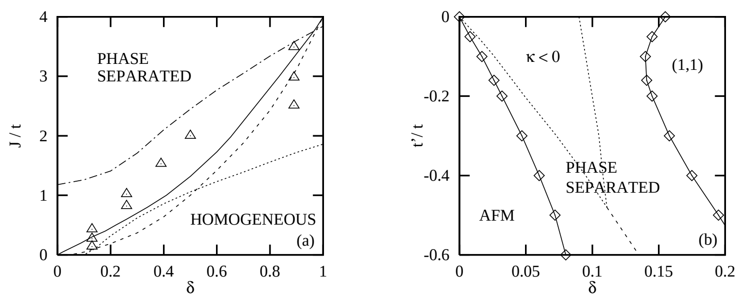

Abb. 1.5: Phase diagram of the t–(t')–J model including phase separated states. The phase separation boundary (solid curve) for the t–J model is shown in the J–δ plane (a). We include the transition lines of Refs. [49] (dashed), [50] (dotted), and [51] (chain dashed). The triangles are the Lanczos results of Ref. [47]. The phase diagram of the t–t'–J is calculated in the t'/t–δ plane at $J/t = 0.4$ (b). Here the two–phase region consists of AFM and (1,1)–spiral states. For further explanation see text.

the Hubbard model [32], the free energy is a convex function $\forall \delta$, i.e., our SRI SB theory does not support recent arguments [47] for phase separation in this limit. In the opposite limit of large J, *complete* charge separation takes place for $J/t > J_{PS}/t = 4.0$, which seems to be an essentially classical result. From exact diagonalization (ED) we obtain $J_{PS}/t = 4.1(\pm 0.1)$ [52], to be compared with $J_{PS}/t = 3.8$ derived by means of a high–temperature expansion [51]. We note that the homogeneous magnetic phases are always unstable close to half–filling (provided $J/t > 0$). This is in qualitative agreement with results obtained from ED studies [47] as well as from semiclassical [49] or renormalization–group calculations [50]. Also plotted in Fig. 1.5 (a) are the results of the high–temperature expansion method [51], where phase separation may occur only above a critical exchange $J/t = 1.2$ as $\delta \longrightarrow 0$, contrary to all the other approaches. The line, separating the two–phase region from the stable states was determined by Marder et al. [49] within a semiclassical theory to vary as $J/t = 4\delta^2$, whereas our theory yields an approximately linear dependence at small δ. We believe that due to an improved treatment of spin correlations in our approach, the region of *incomplete* phase separation is reduced. The instability towards phase separation at small J can be taken as an indication that charge correlations may play an important role as well.

The dotted lines of zero inverse compressibility in Fig. 1.5 (b) show that also for $|t'/t| > 0$ there is a finite range of δ over which the (1,1)–spiral is locally unstable. Similar results were recently obtained by Psaltakis and Papanicolaou [38]. But it is important to stress that in our theory the AFM state is *locally* stable for *both* signs of t'. In addition, based on the Maxwell construction, we can show that near half–filling the AFM state remains also *globally* stable against phase separation for the t–t'–J model (cf. Fig. 1.5 (b), where the two–phase region is bounded by the solid lines). At larger values of $|t'/t| \gtrsim 0.5$, the phase–separated region is due to the first–order nature of the transition AFM$\rightleftharpoons$(1,1)–spiral (dashed curve) [38].

Finally to demonstrate the quality of our SRI SB approach, for the t–J model the expectation value of the kinetic energy is compared with the results from ED for a finite 16–site [48] (36–site [52]) lattice in Fig. 1.6. We

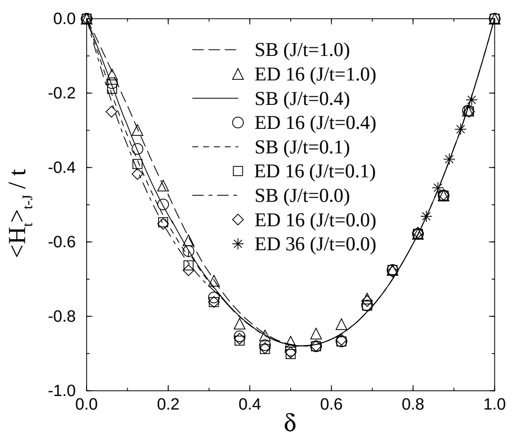

Abb. 1.6: Expectation value of the kinetic energy as a function of doping at several interaction strengths J in comparison to ED results for the 16 (36) site lattice [48, 52].

find an excellent agreement between SB results and ED data. Obviously, this result does not depend on the interaction strength J, i.e. the SB theory well describes important correlation effects. Note that $\langle \mathcal{H}_t \rangle_{t-J}/t$ is directly related to the effective transfer amplitude of the renormalized quasiparticle band, which is taken as input for the calculation of transport coefficients in the following section.

1.3 Comparison with experiments

1.3.1 Normal–state transport properties

As one of the main normal–state puzzles of the CuO_2 based high–T_c superconductors, the anomalous transport properties, in particular the temperature and doping dependence of the Hall resistivity $R_H(T, \delta)$ [53, 54, 55, 56], has been under extensive experimental and theoretical study. Quasiparticle transport measurements suggest a small density of charge carriers and hence a *small* "pocket-like" Fermi surface (FS) [57]. On the other hand, direct (angle–resolved photoemission (ARPES)) probes of the FS [14, 58] yield a *large* FS which satisfies Luttinger's theorem and might be well described by (LDA) band structure calculations [13, 59]. In principle, this contrasting behaviour is found for hole– ($La_{2-x}Sr_xCuO_4$, $YBa_2Cu_3O_{6+x}$) and electron–doped ($Nd_{2-x}Ce_xCuO_4$) copper oxides as well.

Adopting the hypothesis of Trugman [60], most of the normal–state properties of the cuprates may be explained by the dressing of quasiparticles due to magnetic interactions and the subsequent modification of their dispersion relation. Then, once the quasiparticle band $E_{\vec{k}\nu}$ has been obtained, the Hall resistivity $R_H = \sigma_{xyz}/\sigma_{xx}\sigma_{yy}$ can be calculated in the relaxation time approximation, using standard formulas for the transport coefficients:

$$\begin{aligned} \sigma_{\alpha\beta} &= -\frac{e^2\tau}{\hbar^2 V}\sum_{\vec{k}\nu} v_{\alpha\vec{k}\nu} v_{\beta\vec{k}\nu} \frac{\partial n_{\vec{k}\nu}}{\partial E_{\vec{k}\nu}} \, , \\ \sigma_{\alpha\beta\gamma} &= -\frac{e^3\tau^2}{\hbar^4 cV}\sum_{\vec{k}\nu} v_{\alpha\vec{k}\nu}\,\epsilon_{\lambda\kappa\gamma}\, v_{\lambda\vec{k}\nu} \frac{\partial v_{\beta\vec{k}\nu}}{\partial k_\kappa}\frac{\partial n_{\vec{k}\nu}}{\partial E_{\vec{k}\nu}} \, . \end{aligned} \tag{1.3.1}$$

Here $n_{\vec{k}\nu}$ is given by Eq. (1.2.28), V denotes the volume of the unit cell, $\epsilon_{\lambda\kappa\gamma}$ is the completely antisymmetric tensor, and $v_{\alpha\vec{k}\nu} = \partial E_{\vec{k}\nu}/\partial k_\alpha$. Note that R_H does not depend on the relaxation time τ.

To make the discussion more quantitative, let us now consider the doping dependence of $R_H(\delta, T)$ in terms of the t–t'–J model using the saddle–point and relaxation time approximations, where FS and correlation effects are involved via the renormalized SB band $E_{\vec{k}\nu}$ (1.2.31). As we have pointed out above, in our approach the SB quasiparticle band dispersion $E_{\vec{k}\nu}$ has to be determined in a self–consistent way at each doping level δ. This should be contrasted to the NZA SB mean–field approach to the t–t'–J model of Chi and Nagi [61], where, in the $J \rightarrow 0$ limit, the calculation of transport properties is based on the simple replacement $\varepsilon_{\vec{k}} \rightarrow \tilde{\varepsilon}_{\vec{k}} = -2t\delta\,[(\cos k_x + \cos k_y) + 2t'/t\ \cos k_x \cos k_y]$ of the noninteracting band dispersion (1.1.2).

Figure 1.7 shows the theoretical Hall resistivity as a function of carrier density in comparison to experiments on LSCO [53], YBCO [54] and NCCO [55, 56]. In the LSCO and NCCO systems, the concentration of

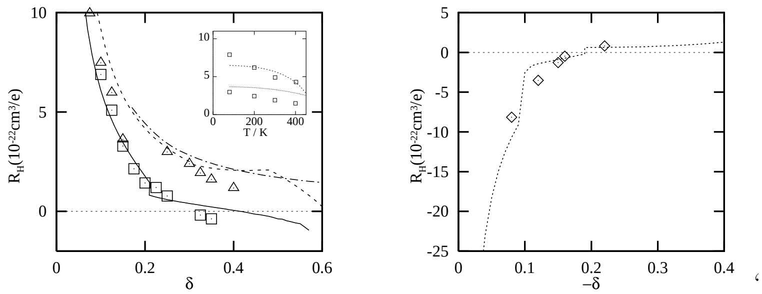

Abb. 1.7: Doping dependence of the Hall resistivity for hole– (left panel) and electron–doped (right panel) systems. The slave–boson results for $J/t = 0.4$ and different ratios $t'/t = 0$ (solid), -0.16 (dashed), -0.4 (chain dotted) and $t'/t = 0.16$ (dotted) are compared with experiments on LSCO (□) [53] [at 80 K], YBCO (△) [54] [at 100 K] and NCCO (◇) [55, 56] [at 80 K], respectively. The inset shows the temperature dependence of R_H for $t'/t = 0$ at $\delta = 0.1$ (short dashed) and $\delta = 0.15$ (dotted).

chemically doped charge carriers in the CuO_2 planes (δ) definitely agrees with the composition (x) of the substitutes Sr and Ce. This simple relation, however, no longer holds for YBCO, i.e., the number of 'holes' transferred into the planes does not increase linearly with the oxygen content. Indeed, the magnetic properties indicate $\delta \simeq 0$ up to $x = 0.2$ [45]. In order to compare our theoretical model with the $R_H(x)$ data found on oxygen doped YBCO, we use the relation $\delta = (x - 0.2)/2$ [62]. Fig. 1.7 clearly demonstrates the importance of the NNN transfer term t' for a consistent theoretical description of the experimental Hall data. For $J/t = 0.4$, an excellent agreement with experiments on LSCO and NCCO, including the sign change of $R_H(\delta)$ at a very similar value, can be achieved using the parameter values $t'/t = 0$ and $t'/t = 0.16$, respectively. It should be noted that in the case of LSCO we obtain $t'/t = 0$ from $R_H(\delta)$ while LDA calculations yield a ratio $t'/t = -0.16$ [13, 59]. For $YBa_2Cu_3O_{6+x}$, where the experiments [54] give $R_H > 0$ up to $x = 1$, a negative t'–term suffices to give the correct tendency to $R_H(\delta)$. Using $t'/t = -0.4$, our theory yields a sign change of R_H at $\delta \sim 0.7$. The strong increase (decrease) of the positive (negative) Hall coefficient as $\delta \to 0$ can be attributed to the formation of small hole (electron) pockets in the FS, which is a correlation effect. A recent analysis of resistivity saturation in LSCO [57], based on Boltzmann transport, has been taken as an indication of a small FS as well, however, the existence of a pocket–like FS is still a subtle and unresolved issue. We found that the temperature dependence of $R_H(\delta, T)$ is at least in qualitative agreement with experiments on LSCO (see inset Fig. 1.7 (left panel)). Note that the quasiparticle dispersion $E_{\vec{k}\pm}$ exhibits extremely *flat* minima implying the presence of a new small energy scale Δ. Therefore, when the temperature becomes comparable to Δ the hole pockets are washed out and a sign change of R_H occurs (cf. Fig. 1.7 at fixed δ (inset)).[3]

The FS of the interacting system are shown in Fig. 1.8 for typical ratios t'/t at $J/t = 0.4$ and $\delta = \pm 0.1$, where the diagonal (1,1)–spiral phase is lowest in energy. As observed for t–J and Hubbard models as well [64], we obtain small hole (or electron) pockets with a volume $\propto |\delta|$. The calculated

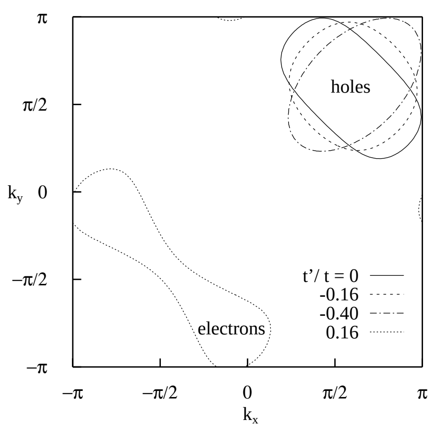

Abb. 1.8: Quasiparticle Fermi surface in the (1,1)–spiral phase at $J/t = 0.4$ for $\delta = 0.1$ (hole–doped system) and $\delta = -0.1$ (electron–doped system).

FS are very anisotropic. As $|\delta|$ increases, the pockets grow, until the FS topology changes completely at a critical doping value δ_c ($R_H(\delta_c) = 0$; cf. Fig 1.7), reflecting the transition from hole to electron carriers for $t'/t < 0$ and vice versa for $t'/t > 0$. We would like to point out here that the renormalization of the quasiparticle band $E_{\vec{k}\nu}$ strongly depends on both interaction strength J and doping level δ [62], which, in fact, calls the frequently used rigid band approximation into question. Due to the strong

[3] We recently learned of a related exact diagonalization study of Dagotto *et al.* [63], where, similar in conclusion, the doping and temperature dependence of R_H was calculated using a strongly renormalized *flat* quasiparticle dispersion.

coupling of spin and charge dynamics the characteristic energy scale for the coherent motion of the charge carriers is J and not t (provided $t > J$).

1.3.2 Magnetic correlations and spin dynamics

In this section, we try to understand the INS and NMR experiments on the basis of the SRI SB mean–field theory. Using a generalized RPA expression for the spin susceptibility and assuming that the AFM correlations are spatially filtered by various $\vec{q}$–dependent hyperfine form factors, we focus, in particular, on the spin *dynamical* properties in the *paraphase* of the t–t'–J model. Our starting point is an RPA–like form for the exchange–enhanced spin susceptibility [5, 6, 65]

$$\chi_s(\vec{q},\omega) = \frac{\overline{\chi}_o(\vec{q},\omega)}{1+\frac{J}{2}(\cos q_x + \cos q_y)\,\overline{\chi}_o(\vec{q},\omega)}\ . \tag{1.3.2}$$

The irreducible part[4]

$$\overline{\chi}_o(\vec{q},i\omega_m) = -\frac{2}{\beta N}\sum_{\vec{k},n}\overline{G}(\vec{k},i\omega_n)\,\overline{G}(\vec{k}+\vec{q},i\omega_{n+m}) \tag{1.3.3}$$

contains the (dressed) SB Green propagators $\overline{G}(\vec{k},i\omega_n) = [i\omega_n - E_{\vec{k}} + \tilde{\mu}]^{-1}$ describing noninteracting electrons with the *renormalized* band structure $E_{\vec{k}}(\delta)$ (1.2.34).

Once the dynamic spin susceptibility has been obtained, both INS measurements and NMR experiments can be explored. From the fluctuation–dissipation theorem the $\vec{q}$– and ω–dependent spin structure factor

$$S(\vec{q},\omega) = \frac{1}{\pi}\,\frac{1}{1-\exp(-\beta\hbar\omega)}\ Im\,\chi_s(\vec{q},\omega) \tag{1.3.4}$$

probed by INS is related to the dynamical susceptibility. On the other hand, the nuclear spin–lattice relaxation rate ${}^aT_{1\alpha}^{-1}$ ($\alpha = \perp, \|$), e.g. for a field H_α applied parallel to the c–axis given by [66]

$$\left({}^aT_{1\|}T\right)^{-1} = \frac{1}{2}\,\frac{k_B}{\mu_B^2\hbar}\lim_{\omega\to 0}\frac{1}{N}\sum_{\vec{q}}{}^aF_\perp^2(\vec{q})\ \frac{Im\,\chi_s(\vec{q},\omega)}{\hbar\omega} \tag{1.3.5}$$

and the transverse spin–spin relaxation rate, T_{2G}^{-1}, for the RKKY coupling

[4] $\omega_n = 2n\pi/\beta$ [$\omega_m = (2m+1)\pi/\beta$] denote the fermionic [bosonic] Matsubara frequencies

of the nuclear Cu spins given by [67]

$$T_{2G}^{-2} = \frac{c}{8\hbar^2(2\mu_B)^4}\left[\frac{1}{N}\sum_{\vec{q}}\left(F_{\parallel}^2(\vec{q})\,\chi_s(\vec{q})\right)^2 - \left(\frac{1}{N}\sum_{\vec{q}}F_{\parallel}^2(\vec{q})\,\chi_s(\vec{q})\right)^2\right], \tag{1.3.6}$$

provide local, atomic site ($a = \{63, 17\}$) specific information. Here μ_B denotes the Bohr magneton and the constant $c = 0.69$ is the natural–abundance fraction of the ^{63}Cu isotope. The form factors are given for ^{63}Cu and the planar ^{17}O nucleus as [68]

$$\begin{aligned} {}^{63}F_\alpha(\vec{q}) &= A_\alpha + 2B(\cos q_x + \cos q_y)\,, && (1.3.7)\\ {}^{17}F_\alpha(\vec{q}) &= 2\,C\,\cos\tfrac{q_x}{2}\,. && (1.3.8)\end{aligned}$$

Together with the anisotropy of the Cu relaxation rates the measurements of the Knight shift, ${}^aK_\alpha = \frac{2}{\mu_B{}^a\gamma_n}\lim_{\vec{q}\to 0}{}^aF_\alpha(\vec{q})\,\chi_s(\vec{q},\omega=0)$, have been used to determine the hyperfine coupling constants A_α, B and C on the basis of the Mila–Rice Hamiltonian [69]. Following Ref. [66] we take $A_\parallel \approx -4B$, $A_\perp \approx 0.84B$, $C \approx 0.87B$ and $B \approx 3.3\;10^{-7}$ eV, where ${}^{63}\gamma\hbar = 7.5\;10^{-24}$ erg/G and ${}^{17}\gamma\hbar = 3.8\;10^{-24}$ erg/G.

As we know, the RPA susceptibility contains an unphysical instability of the paramagnetic phase at some particular wave–vector $\vec{q}$ below a critical doping δ_c as signaled by the zero in the denominator of (1.3.2) at $\omega = 0$ (Stoner condition). Therefore the use of (1.3.2) only makes sense if the system is far from the magnetic instability, i.e., $\delta > \delta_c$, where for $J = 0.4$ we have $\delta_c(t'/t = -0.16) \simeq 0.27$ and $\delta_c(-0.4) \simeq \delta_c(0) \simeq 0.17$.

Inelastic neutron scattering measurements. We begin with a discussion of the RPA dynamical spin structure factor $S(\vec{q},\omega)$. The $\vec{q}$–dependence of $S(\vec{q},\omega)$ along the main symmetry axis of the Brillouin zone is shown in Fig. 1.9 at $J = 0.4$ and hole density $\delta = 0.3$ for different ratios t'/t. Here the temperature is $T = 35$ K and the frequency $\hbar\omega = 10$ meV. For LSCO–type parameters ($t'/t = 0$, -0.16) we found four pronounced incommensurate peaks located at the points $\pi(1 \pm q_o, 1)$, $\pi(1, 1 \pm q_o)$. The incommensurate modulation wave–vectors move with increasing doping level δ away from the corner of the Brillouin zone along the directions $(1,\pi)$ or $(\pi,1)$ (square lattice notation). Note that while the incommensurate peak position obtained from a three–band RPA calculation of $S(\vec{q},\omega)$ [5] can be parametrized consistent with the experimental observation that $q_o \simeq 2x$ [37], all the effective one–band RPA approaches [6, 10] yield an incommensurability scaling rather as $q_o \simeq \delta$. A more detailed investigation of the LSCO–type $\vec{q}$–scans show that the $\vec{q}$–variation of $S(\vec{q},\omega)$ is mainly governed by that of $\overline{\chi}_o(\vec{q},\omega)$

and, in accordance with experiments [70], the incommensurate peaks considerably broaden as temperature or energy transfer are increased [71]. By contrast, the same plot for YBCO–type ($t'/t = -0.4$) parameters shows a broad, nearly T–independent [71], maximum around the (π, π) point [72] (see Fig. 1.9) which, due to the flat topology of $\overline{\chi}_o$, mainly reflects the $\vec{q}$–dependence of $J(\vec{q}) = J(\cos q_x + \cos q_y)$ (cf. Eq. (1.3.2)). In this way, our

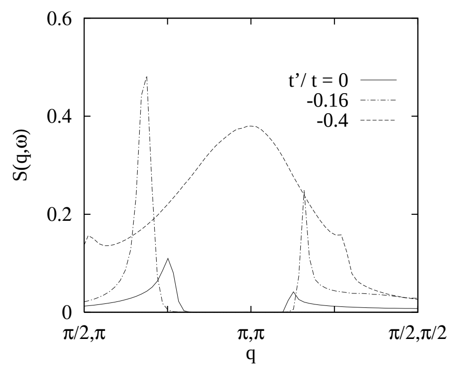

Abb. 1.9: Dynamic magnetic structure factor $S(\vec{q}, \omega)$ is plotted along the (1,1)– and $(1, \pi)$–directions of the Brillouin zone for different ratios t'/t.

calculations confirm recent arguments [5, 73, 6] for the importance of band structure (Fermi–surface geometry) effects in explaining the difference between observed LSCO and YBCO spin dynamics. Nevertheless, whether the incommensurate signals arise from an intrinsic magnetic structure or whether they result from the formation of domains (charge superstructures) in the LSCO system remains unanswered by INS [2, 68].

In a next step, we calculate the longitudinal or spin–lattice relaxation rate, T_1^{-1}, using the hyperfine form factors (1.3.8). In Fig. 1.10 the tempe-

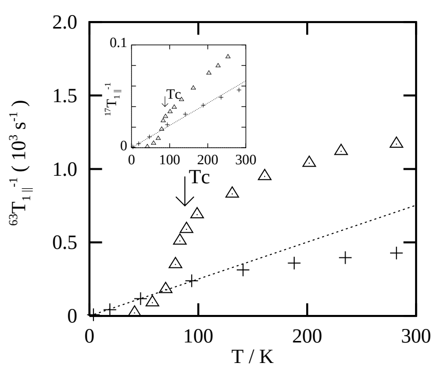

Abb. 1.10: Spin–lattice relaxation rates $^{63}T_{1\|}^{-1}$ and $^{17}T_{1\|}^{-1}$ (inset) as a function of temperature. SB results ((+); $t'/t = -0.4$, $\delta = 0.35$) are compared with experiments ($\triangle$) on $YBa_2Cu_3O_7$ [74].

rature dependences of $^{63}T_{1\|}^{-1}$ and $^{17}T_{1\|}^{-1}$ (inset) are shown for $\delta = 0.35$ and $t'/t = -0.4$ in comparison to experiments [74] on fully oxygenated YBCO materials ($x = 1$). Although our theory does not succeed in giving the correct amplitude of ${}^{a}T_{1\|}^{-1}$ the qualitative features of the NMR data are described surprisingly well. Obviously, the broad magnetic peak in $S(\vec{q}, \omega)$ at the AFM wave–vector $\vec{Q}_{AFM} = (\pi, \pi)$ strongly enhances the relaxation rate on Cu sites while, due to a geometrical cancellation (${}^{17}F_{\alpha}(\vec{q} \simeq \vec{Q}_{AFM}) \simeq 0$), the corresponding oxygen rate is rather insensitive to nearly commensurate AFM fluctuations, and therefore is governed by the long wavelength part $\vec{q} \simeq 0$ of the spin susceptibility [2]. For ^{63}Cu the nominal Korringa ratio $S \equiv (1/T_1 T K_S^2)$ (K_S denotes the spin part of the Knight shift) is at least one order of magnitude larger. As can be seen from Fig. 1.10, for $YBa_2Cu_3O_7$–type parameters, a Korringa ($1/T_1 \propto T$) dependence (dotted line) holds at both Cu and O sites below $T^* \sim 120$ K, demonstrating the existence of a characteristic temperature T^* as well as in all other near–optimum–T_c compounds [2, 75]. T^* is in good agreement with the coherence energy scale suggested experimentally [75]. Above T^* the ^{17}O NMR relaxation remains linear whereas the ^{63}Cu relaxation time does not follow the Korringa law.

In the oxygen–deficient compound $YBa_2Cu_3O_{6.6}$, $1/({}^{63}T_{1\|}T)$ shows a broad maximum at about 150 K (see Fig. 1.11), which reflects a strong deviation from the canonical Korringa behaviour. In the normal state re-

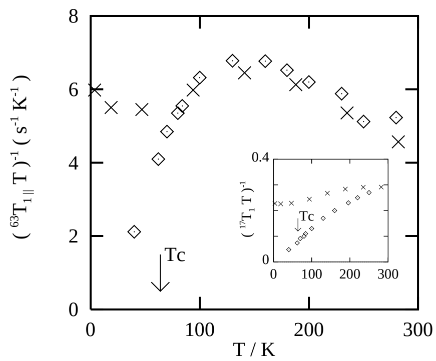

Abb. 1.11: ^{63}Cu and planar ^{17}O relaxation data ($\diamond$) for underdoped $YBa_2Cu_3O_{6.6}$[76] are plotted *vs* temperature. Theoretical results ($\times$) are given at $t'/t = -0.4$, and $\delta = 0.2$.

gime the theoretical results agree even quantitatively with the experimental ^{63}Cu–NMR data [76]. At this point it is important to stress that the present theory incorporates considerable band renormalization effects already via $\overline{\chi}_o(\vec{q}, \omega)$, especially, at low doping level. Thus a rather moderate strength $J = 0.4$ of the AFM exchange interaction yields the experimentally observed enhancement of ${}^{63}T_{1\|}$. In striking contrast to the optimally doped YBCO system, the Korringa relation is no longer satisfied for the planar ^{17}O nucleus sites in the underdoped material (cf. inset Fig. 1.11). Instead, a different behaviour $^{17}T_{1\|}T^{17}K_S = const$ was suggested to hold down to T_c [76]. The unconventional T–scaling of $^{17}T_{1\|}$ has been taken as a signature for another important feature of the normal–state spin dynamics, the so–called spin–gap behaviour [2].

Complementary measurements of the transverse spin–spin relaxation rate, T_{2G}^{-1}, have provided further insights into the drastic change in the magnetic properties when passing from the overdoped to the underdoped regime [67, 77]. As experimentally observed, we found that T_{2G}^{-1} increa-

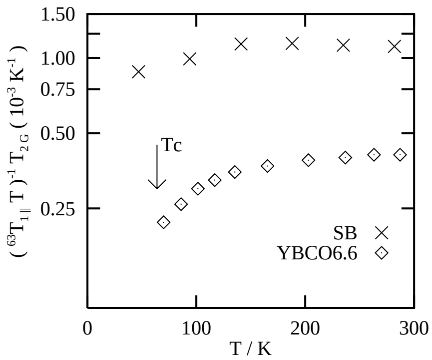

Abb. 1.12: $T_{2G}/(^{63}T_{1\|}T)$ in $YBa_2Cu_3O_{6.6}$ ($\diamond$) as measured by Takigawa [67] compared with the SB data ($\times$) at $t'/t = -0.4$, and $\delta = 0.2$.

ses (decreases) with increasing (decreasing) hole doping (temperature) [78]. In order to detect the opening of a spin–pseudogap as a function of T, a powerful technique is to measure the ratio T_{2G}/T_1T [79] which is nearly constant above ~ 200 K for desoxygenated $YBa_2Cu_3O_{6.6}$ [67]. The calculated temperature dependence of this quantity is shown in Fig. 1.12 together with recent experimental results [67]. Most noticeably, the opening of a spin–pseudo gap at $T^\star \simeq 135$ K [79], i.e. well above T_c, is clearly seen as a decrease of T_{2G}/T_1T below $T^\star$. Note that for $YBa_2Cu_3O_7$, as predicted by Fermi liquid theories, the ratio T_{2G}^2/T_1T is approximately constant above 150 K [2].

1.4 Summary

In this work we have used a spin–rotation–invariant SB approach to investigate magnetic and transport properties of the 2D t–t'–J model. Our main results are the following:

(i) We present a detailed magnetic ground–state phase diagram of the 2D t–(t')–J model, including incommensurate magnetic structures and phase separated states. At finite t', a main feature of the phase diagram, we would like to emphasize, is the existence of an AFM state away from half filling, which is locally and also globally stable against phase separation. This result agrees with the experimentally observed AFM long–range order in the weakly doped LSCO and YBCO compounds. In contrast, for the simple t–J model we observe no AFM long range order at any finite doping due to phase separation.

(ii) The next nearest–neighbour hopping process (t') incorporates important correlation and band structure effects near half–filling. In particular, the t'–term can be used to reproduce the FS geometry of LSCO, YBCO, and NCCO. Also the NNN hopping provides a possible origin for the experimentally observed asymmetry in the persistence of AFM order of hole– and electron–doped systems.

(iii) The quality of the SRI SB approach was demonstrated in comparison with exact diagonalization results available for the t–J model on finite square lattices with up to 36 sites. In this case, the SB method yields an excellent estimate for the quasiparticle band renormalization.

(iv) Within the saddle–point and relaxation–time approximation, our SB calculation of the Hall resistivity in the t–t'–J model provides a reasonable explanation of the experimentally observed doping dependence of R_H on both hole– ($La_{2-x}Sr_xCuO_4$, $YBa_2Cu_3O_{6+x}$) and electron–doped ($Nd_{2-x}Ce_xCuO_4$) copper oxides.

(v) Using a generalized RPA expression for the spin susceptibility and assuming that the AFM correlations are spatially filtered by the hyperfine form factors, we have calculated the temperature dependences of spin–lattice and spin–spin relaxation rates for planar copper and oxygen sites, the results agree qualitatively well with various NMR experiments on $YBa_2Cu_3O_{6+x}$. In addition, we can attribute the contrasting $\vec{q}$–dependence of the magnetic structure factor $S(\vec{q},\omega)$ seen in INS experiments for LSCO– and YBCO–type systems to differences in their fermiology.

Recently, our theory was improved to include (Gaussian) fluctuations beyond the paramagnetic saddle–point approximation [80, 27], We derived a concise expression for the spin susceptibility $\chi_s(\vec{q},\omega)$ of the t–t'–J model, which does not have the standard RPA form. Then we were able to show that the instability line obtained from a divergence of $\chi_s(\vec{q},0)$ is in agreement with the PM$\rightleftharpoons$spiral–state phase boundary in the saddle–point phase diagram (which in fact proves the consistency of both approaches [27]).

Bibliography

[1] For a recent overview of the experimental and theoretical situation see *Proceedings of the Int. Conf. M^2S HTSC IV*, Grenoble 1994, in Physica C **235**–**240** (1994), and *Proceedings of the Int. Euroconf. on Magnetic Correlations, Metal–Insulator-Transitions, and Superconductivity*, Würzburg 1994, in J. Low. Temp. Phys. **3/4** (1995).

[2] A. P. Kampf, Physics Reports **249**, 219 (1994).

[3] A. J. Millis and H. Monien, Phys. Rev. Lett. **70**, 2810 (1993).

[4] P. Monthoux and D. Pines, Phys. Rev. B **49**, 4261 (1941).

[5] Q. Si, Y. Zha, K. Levin, and J. P. Lu, Phys. Rev. B **47**, 9055 (1993).

[6] T. Tanamoto, K. Kuboki, and H. Fukuyama, J. Phys. Soc. Jpn. **60**, 3072 (1991); T. Tanamoto, H. Kohno, and H. Fukuyama, J. Phys. Soc. Jpn. **62**, 717 (1993); **62**, 1455 (1993); **63** 2739 (1994).

[7] T. Ito, K. Takenaka, and S. Uchida, Phys. Rev. Lett. **70**, 3995 (1993).

[8] V. J. Emery, Phys. Rev. Lett. **58**, 2794 (1987).

[9] M. S. Hybertsen, M. Schlüter, and N. E. Christensen, Phys. Rev. B **39**, 9028 (1989).

[10] P. Bénard, L. Chen, and A.-M. S. Tremblay, Phys. Rev. B **47**, 15217 (1993).

[11] M. Lavagna and G. Stemmann, Phys. Rev. B **49**, 4235 (1994).

[12] T. Tohyama and S. Maekawa, Phys. Rev. B **49**, 3596 (1994).

[13] J. Yu, S. Massida, and A. J. Freeman, Phys. Lett. A **122**, 198 (1987).

[14] D. M. King et al., Phys. Rev. Lett. **70**, 3159 (1993).

[15] P. A. Lee, Phys. Rev. Lett. **63**, 680 (1989).

[16] D. M. News, M. Rasolt, and P. Pattnik, Phys. Rev. B **38**, 6513 (1988).

[17] Z. Zou and P. W. Anderson, Phys. Rev. B **37**, 627 (1988).

[18] D. Yoshioka, J. Phys. Soc. Jpn. **58**, 1516 (1989).

[19] H. Kaga, Phys. Rev. B **46**, 1979 (1992).

[20] S. K. Sarker, Phys. Rev. B **47**, 2940 (1993).

[21] J. Igarashi and P. Fulde, Phys. Rev. B **48**, 998 (1993).

[22] Y. M. Li, D. N. Sheng, Z. B. Su, and L. Yu, Phys. Rev. B **45**, 5428 (1992).

[23] S. D. Liang, B. Doucot, and P. W. Anderson, Phys. Rev. Lett. **61**, 365 (1988).

[24] G. Kotliar and A. E. Ruckenstein, Phys. Rev. Lett. **57**, 1362 (1986).

[25] R. Frésard and P. Wölfle, Int. J. Mod. Phys. B **5&6**, 685 (1992); Erratum *ibid.* 3087 (1992)

[26] M. Deeg, H. Fehske, and H. Büttner, Europhys. Lett. **26**, 109 (1994).

[27] M. Deeg and H. Fehske, Phys. Rev. B **50**, 17874 (1994).

[28] T. Li, P. Wölfle, and P. J. Hirschfeld, Phys. Rev. B **40**, 6817 (1989).

[29] J. W. Negele and H. Orland, *Quantum Many-Particle Systems*, Addison–Wesley, (Reading, MA 1988).

[30] T. Jolicoeur and J. C. L. Guillou, Phys. Rev. B **44**, 2403 (1991).

[31] E. Arrigoni et al., Physics Reports **241**, 291 (1994).

[32] M. Deeg, H. Fehske, and H. Büttner, Z. Phys. B **88**, 283 (1992).

[33] L. Lilly, A. Muramatsu, and W. Hanke, Phys. Rev. Lett. **65**, 1379 (1990).

[34] R. Frésard, M. Dzierzawa, and P. Wölfle, Europhys. Lett. **15**, 325 (1991); E. Arrigoni and G. C. Strinati, Phys. Rev. B **44**, 7455 (1991).

[35] B. Möller, K. Doll, and R. Frésard, J. Phys. Condens. Matter **5**, 4847 (1993).

[36] D. Boies, F. A. Jackson, and A.-M. S. Tremblay, Int. J. Mod. Phys. B **9**, 1001 (1995).

[37] S.-W. Cheong et al., Phys. Rev. Lett. **67**, 1791 (1991).

[38] G. C. Psaltakis and N. Papanicolaou, Phys. Rev. B **48**, 456 (1993).

[39] H. Mori and M. Hamada, Phys. Rev. B **48**, 6242 (1993).

[40] A. P. Kampf and W. Brenig, J. Low Temp. Phys. **95**, 335 (1994).

[41] V. Chechersky et al., Phys. Rev. Lett. **70**, 3355 (1993).

[42] M. Matsuda et al., Phys. Rev. B **45**, 12548 (1992).

[43] G. M. Luke et al., Phys. Rev. B **42**, 7981 (1990).

[44] T. R. Thurston et al., Phys. Rev. B **40**, 4585 (1990).

[45] J. Rossat-Mignod et al., Physica B **180 & 181**, 383 (1992).

[46] V. J. Emery and S. A. Kivelson, Physica C **209**, 597 (1993).

[47] V. J. Emery, S. A. Kivelson, and H. Q. Lin, Phys. Rev. Lett. **64**, 475 (1990).

[48] H. Fehske, V. Waas, H. Röder, and H. Büttner, Phys. Rev. B **44**, 8473 (1991).

[49] M. Marder, N. Papanicolaou, and G. C. Psaltakis, Phys. Rev. B **41**, 6920 (1990).

[50] E. V. L. de Mello, J. Phys. Condens. Matter **6**, 117 (1994).

[51] W. O. Puttika, M. Luchini, and T. M. Rice, Phys. Rev. Lett. **68**, 538 (1992).

[52] V. Waas, H. Fehske, and H. Büttner, Phys. Rev. B **48**, 9106 (1993).

[53] H. Takagi et al., Phys. Rev. B **40**, 2254 (1989).

[54] E. C. Jones et al., Phys. Rev. B **47**, 8986 (1993).

[55] H. Takagi, S. Uchida, and Y. Tokura, Phys. Rev. Lett. **62**, 1197 (1989).

[56] S. J. Hagen, J. L. Peng, Z. Y. Li, and R. L. Greene, Phys. Rev. B **43**, 13606 (1991).

[57] H. Takagi et al., Phys. Rev. Lett. **69**, 2975 (1992).

[58] J. C. Campuzano et al., Phys. Rev. Lett. **64**, 2308 (1990).

[59] W. E. Pickett, Rev. Mod. Phys. **61**, 433 (1989).

[60] S. A. Trugman, Phys. Rev. Lett. **65**, 500 (1990).

[61] H. Chi and A. D. S. Nagi, Phys. Rev. B **46**, 421 (1992).

[62] H. Fehske and M. Deeg, Solid State Commun. **93**, 41 (1995).

[63] E. Dagotto, A. Nazarenko, and M. Bonsinsegni, Phys. Rev. Lett. **73**, 728 (1994).

[64] S. Sarker, C. Jayaprakash, H. R. Krishnamurthy, and W. Wenzel, Phys. Rev. B **43**, 8775 (1991).

[65] R. Grempel and M. Lavagna, Solid State Commun. **83**, 595 (1992).

[66] H. Monien, P. Monthoux, and D. Pines, Phys. Rev. B **42**, 167 (1990).

[67] M. Takigawa, Phys. Rev. B **49**, 4158 (1994).

[68] V. Barzykin, D. Pines, and D. Thelen, Phys. Rev. B **50**, 16052 (1994).

[69] F. Mila and T. M. Rice, Physica C **157**, 561 (1989).

[70] T. E. Mason, G. Aeppli, and H. A. Mook, Phys. Rev. Lett. **68**, 1414 (1992).

[71] H. Fehske and M. Deeg, J. Low Temp. Phys. **3/4**, 425 (1995).

[72] J. Rossat-Mignod et al., Physica C **185–189**, 86 (1991).

[73] P. Littlewood, J. Zaanen, G. Aeppli, and H. Monien, Phys. Rev. B **48**, 487 (1993).

[74] M. Takigawa et al., Physica C **162**, 853 (1989).

[75] P. C. Hammel et al., Phys. Rev. Lett. **63**, 1992 (1989).

[76] M. Takigawa et al., Phys. Rev. B **43**, 247 (1991).

[77] Y. Itoh et al., J. Phys. Soc. Jpn. **61**, 1287 (1992).

[78] M. Deeg, PhD thesis, University of Bayreuth, (1995).

[79] C. Berthier et al., Physica C **235–240**, 67 (1994).

[80] M. Deeg et al., Z. Phys. B **95**, 87 (1994).